40th Fluid Dynamics Conference and Exhibit
28 June - 1 July 2010, Chicago, Illinois

AIAA 2010-4446

Numerical Study of Hypersonic Receptivity with Thermochemical Non-Equilibrium on a Blunt Cone

Neal Parsons*, Xiaolin Zhong†, John Kim‡, Jeff Eldredge§
University of California, Los Angeles, CA 90095

There is renewed interest in physical phenomena leading to laminar-turbulent transition in hypersonic boundary layers. In high-temperature flows characteristic of hypersonic vehicles, the degree of chemical and thermal non-equilibrium becomes significant. However, not many studies have been conducted on the non-equilibrium effect on the receptivity process to free-stream acoustic disturbances. The goal of this paper is, first, to present a code capable of accurately modeling free-stream acoustic disturbances with non-equilibrium effects, and, second, to present preliminary findings on the non-equilibrium effects on receptivity. This is done by examining Mach 15.3 flow over a blunt cone with nose radius $6.35 \times 10^{-3}\ m$ and half angle 7° and imposing free-stream fast acoustic wave disturbances using a high-order shock-fitting finite-difference solver. Results were computed for flows using both thermochemical non-equilibrium and perfect gas models and were then compared to determine the non-equilibrium effects. Complex wave structures were found in the boundary layer for each gas model when a free-stream acoustic disturbance wave was introduced. The non-equilibrium gas case was found to have higher perturbation amplitudes and had its maximum perturbation amplitude nearer to the blunt nose.

Nomenclature

E	Internal energy J
E_V	Vibrational energy J
F_i	Inviscid flux vector
F_{vi}	Viscous flux vector
$Q_{T-V,s}$	Rate of species vibrational energy increase J/s
R_{univ}	Universal gas constant, 8.314472 $J/(K-mol)$
R	Gas constant $J/(K-kg)$
T	Temperature K
T_V	Vibrational temperature K
U	State vector
W	Source term vector
a	Speed of sound m/s
c	Mass fraction
$e_{V,s}$	Species specific vibrational energy J/kg
h_s	Species specific enthalpy J/kg
k	Thermal conductivity $W/(m-K)$
k_V	Vibrational energy conductivity $W/(m-K)$
n	Normal unit vector
p	Pressure Pa
r	Blunt cone nose radius m
u	Velocity m/s
v_s	Diffusion velocity m/s
w_s	Rate of species creation $kg/(m^3-s)$

*Graduate Student, Mechanical and Aerospace Engineering Department, nparsons@ucla.edu, AIAA member
†Professor, Mechanical and Aerospace Engineering Department, xiaolin@seas.ucla.edu, AIAA Associate fellow
‡Professor, Mechanical and Aerospace Engineering Department; jkim@seas.ucla.edu, AIAA member
§Associate Professor, Mechanical and Aerospace Engineering Department, eldredge@seas.ucla.edu, AIAA member

γ	Ratio of specific heats
μ	Viscosity $kg/(m-s)$
ρ	Density kg/m^3
τ	Viscous stress N/m^2
Subscripts	
∞	Free-stream
i, j, k	Direction i, j, k
s	Species s
V	Vibrational energy component
w	Wall surface

I. Introduction

UNDERSTANDING of laminar-turbulent transition and hypersonic turbulent boundary-layer (HTBL) flows is critically important to the design and operation of hypersonic vehicles. However, very little is understood on the fundamental physics of transitional and turbulent hypersonic boundary layers. In hypersonic flows, temperatures behind a shock rise to values high enough to cause the components of air to react and even ionize. For five-species air without ionization, there are 17 chemical reactions to consider. Among these, some reactions are exothermic and others endothermic, leading to varying effects on flowfield parameters within the boundary layer, and thus, with boundary receptivity and stability. Additionally, different modes of energy do not come to equilibrium across the shock. For instance, there is a relaxation process to bring the vibrational and rotational modes of energy of molecules to thermal equilibrium. The effect of these fundamental phenomena characteristic of hypersonic flow on receptivity and transition to turbulence in hypersonic boundary layers is still relatively unknown. Laboratory experiments are extremely difficult, expensive, and mostly limited to low Mach numbers. Furthermore, relatively few numerical simulations of a hypersonic laminar-turbulent transition are available in the literature. Most of the existing studies were conducted at low Mach numbers and with perfect gas models only. We have implemented a high-order shock-fitting routine for DNS of transitional and turbulent hypersonic flows with non-equilibrium real gas effects. The objective of this paper is to perform DNS studies of the fundamental physics of hypersonic boundary layer receptivity with thermo-chemical non-equilibrium to determine their effect on the receptivity process.

Among the early investigations into the laminar-turbulent transition within hypersonic boundary layers, Mack [1] first found acoustic instability modes in addition to the first-mode instability waves in high Mach number boundary layer flows. It was found that the second Mack mode becomes the dominant instability within hypersonic boundary layers. Malik [2], Stuckert and Reed [3], Hudson et al. [4], and Johnson and Candler [5] studied equilibrium and non-equilibrium real gas effects on linear stability of hypersonic boundary layers. It was found that the dissociation of air species stabilizes the first mode instability, while destabilizing the second mode. The second mode instability shifts to lower frequencies due to the real gas effects. Germain and Hornung [6] experimentally studied the real gas effects on transition location for high enthalpy hypersonic flow over a cone for Mach = 4.7 - 6.5. It was found that transition Reynolds numbers increased for higher total enthalpy. Martin and Candler [7] performed DNS of reacting isotropic turbulence decay under conditions typical of hypersonic turbulent boundary layer flow. Ma and Zhong [8] studied the receptivity of free stream disturbances of a Mach 10 non-equilibrium oxygen flow over a flat plate. They found strong non-equilibrium effects on receptivity, namely that the unstable region for non-equilibrium flow has a greater peak amplitude and longer unstable second Mack mode region. This implies that the real gas effect is destabilizing for the discrete wave modes. However, they did not consider thermal non-equilibrium effects. Stemmer [9] investigated the differences in spatial disturbance development in flat-plate boundary layer flow for Mach = 20 between ideal gas and thermal and chemical non-equilibrium flows using a hybrid-ENO finite volume scheme. Most of these studies are centered on linear instability.

Hypersonic vehicles possess blunt noses in order to reduce the high degree of thermal heating encountered at hypersonic speeds. As such, a fundamental case in the practical study of boundary layer stability and transition has centered on blunt cone geometries. There are many documented computational studies on the study of boundary layer instability both using linear stability analysis to predict unstable modes and regions and direct numerical simulation of the receptivity process. It has been found that there is a complex development of wave structures in hypersonic boundary layers on blunt cones subject to free-stream acoustic disturbances. There are also distinct synchronization locations between different wave modes that play an important role in the receptivity of the unstable second Mack mode in the boundary layer [10 11 12].

There has yet to be a published study on the receptivity of free-stream disturbances on hypersonic boundary layers with thermal and chemical non-equilibrium over blunt bodies. The receptivity of hypersonic boundary layers to free-stream disturbances is significantly altered by the presence of a bow shock in flows over blunt bodies. The main focus of this study is to examine the effects of thermal and chemical non-equilibrium on the receptivity process in the presence of free-stream acoustic waves. We will study the receptivity process for hypersonic boundary layers over a blunt cone with thermal and chemical non-equilibrium. This will be done by computing the steady mean-flow for Mach 15.3 air over a blunt cone with nose radius 6.35×10^{-3} m and half-angle 7°. The solutions will be obtained using a 3^{rd}-order finite-difference shock-fitting routine developed by Zhong [13] for ideal gas flow and modified by Prakash et. al [14] for non-equilibrium flows. The receptivity process will then be examined by introducing a free-stream acoustic wave. These results will be compared to results obtained for the ideal gas model given the same flow parameters to examine the effect of thermal and chemical non-equilibrium.

This paper will detail the governing equations and physical model used and show the steady mean-flow results for the case studied. Then the procedure for introducing free stream waves will be outlined. Finally, results will be presented and investigated for the receptivity to a free-stream fast acoustic wave.

II. Governing Equations and Physical Model

The governing equations for the non-equilibrium gas case are formulated for a two-temperature model with the rotational energy mode assumed fully excited and five non-ionizing species with finite rate chemistry. The conservative three-dimensional Navier-Stokes equations consist of five mass conservation equations, three momentum conservation equations, the vibrational energy conservation equation, and the global energy conservation equations:

$$\frac{\partial U}{\partial t}+\frac{\partial F_j}{\partial x_j}+\frac{\partial F_{vj}}{\partial x_j}=W, \tag{1}$$

where U is the state vector of conserved quantities, W the source terms as defined by

$$U=\begin{bmatrix}\rho_{N_2}\\ \rho_{O_2}\\ \rho_{NO}\\ \rho_{N}\\ \rho_{O}\\ \rho u_1\\ \rho u_2\\ \rho u_3\\ E_V\\ E\end{bmatrix},\qquad W=\begin{bmatrix}w_{N_2}\\ w_{O_2}\\ w_{NO}\\ w_{N}\\ w_{O}\\ 0\\ 0\\ 0\\ \sum\limits_{s=mol.}^{mol.}\left(Q_{T-V,s}+w_s e_{V,s}\right)\\ 0\end{bmatrix}, \tag{2}$$

the flux is split into its viscous, diffusive components F_{vj} and inviscid, convective components F_j

$$F_j=\begin{bmatrix}\rho_{N_2}u_j\\ \rho_{O_2}u_j\\ \rho_{NO}u_j\\ \rho_{N}u_j\\ \rho_{O}u_j\\ \rho u_1u_j+p\delta_{1j}\\ \rho u_2u_j+p\delta_{2j}\\ \rho u_3u_j+p\delta_{3j}\\ E_Vu_j\\ (E+p)\,u_j\end{bmatrix},\qquad F_{vj}=\begin{bmatrix}\rho_{N_2}v_{N_2j}\\ \rho_{O_2}v_{O_2j}\\ \rho_{NO}v_{NOj}\\ \rho_{N}v_{Nj}\\ \rho_{O}v_{Oj}\\ \tau_{j1}\\ \tau_{j2}\\ \tau_{j3}\\ k_V\frac{\partial T_V}{\partial x_j}+\rho\sum\limits_{s=mol.}e_{V,s}v_{sj}\\ \tau_{ji}u_j+k\frac{\partial T}{\partial x_j}+k_V\frac{\partial T_V}{\partial x_j}+\rho\sum\limits_{s}h_sv_{sj}\end{bmatrix}, \tag{3}$$

where the viscous stress is modeled by

$$\tau_{ji} = \mu \left(\frac{\partial u_i}{\partial x_j} + \frac{\partial u_j}{\partial x_i} \right) - \frac{2}{3} \left(\mu \frac{\partial u_k}{\partial x_k} \right) \delta_{ji}. \tag{4}$$

Vibrational energy is determined using the harmonic oscillator model, where $\theta_{V,s}$ is the characteristic vibrational temperature,

$$E_V = \sum_s \rho_s e_{V,s} = \sum_s \rho_s \frac{R_{univ}}{M_s} \frac{\theta_{V,s}}{e^{\theta_{V,s}/T_v} - 1}. \tag{5}$$

The source terms include the creation of species w_s through chemical reaction and vibrational-to-translational energy exchange $Q_{T-V,s}$. The $Q_{T-V,s}$ term is determined using the Landau-Teller formulation,

$$Q_{T-V,s} = \rho_s \frac{e^*_{V,s}(T) - e_{V,s}}{\tau_{V,s}}. \tag{6}$$

where $e^*_{V,s}(T)$ represents the species specific vibrational energy computed using the translational temperature and the relaxation time $\tau_{V,s}$ is given by Millikan and White[15]. In the 5-species model, there are 17 unique chemical reactions that take place:

$$\begin{array}{l} N_2 + M \Leftrightarrow 2N + M \\ O_2 + M \Leftrightarrow 2O + M \\ NO + M \Leftrightarrow N + O + M \\ N_2 + O \Leftrightarrow NO + N \\ NO + O \Leftrightarrow O_2 + N \\ M \in [N_2, O_2, NO, N, O]\,. \end{array} \tag{7}$$

The reaction rates k_f and k_b in Eqs. (8)- (9) are determined using Park's[16,17] two-temperature model. In this model, the defining reaction temperature for the forward rates is $T_a = \sqrt{TT_V}$ for dissociating species, and $T_a = T$ for exchange reactions and recombination reactions. The equilibrium constants K_{eq} are determined using the Gibbs free energy approach, Eq. (10), with curve-fit expressions for species thermodynamic properties[18].

$$k_f = C_f T_a^{\eta} \exp(-\theta_d / T_a) \tag{8}$$

$$k_b = K_{eq} / k_f \tag{9}$$

$$K_{eq} = e^{\frac{-\Delta_f G^o}{RT}} \tag{10}$$

The viscous transport parameters, including global viscosity μ, global thermal conductivity k, and vibrational energy conductivity k_V, are computed using the Yos mixing rules with curve-fit coefficients given by Gupta et. al[19]. The species diffusive velocities v_{sj} are determined by Ramshaw's self-consistent effective binary diffusion model[20]. It is noted that there are many different modes of energy to be considered in modeling non-equilibrium flows, and, further, different models to represent those modes. The formulation of these governing equations with the presented physical models merely one of many ways to model non-equilibrium flows.

To compute the flow using a perfect gas model, the source term vector W is removed from Eq. 1 and all T_V and E_V terms are removed from the governing equations.

The equations are solved using Zhongs high-order shock-fitting code, capable of 3^{rd}-order temporal accuracy and 3^{rd}-order spatial accuracy[13]. The shock-fitting method treats the shock as a computational boundary. Flow variables across the shock are computed by the Rankine-Hugoniot relations and a characteristic compatibility equation from behind the shock, which takes into account transient shock movement and shock interaction with free-stream disturbances. For simplicity, ionization, radiation, surface chemistry, and in-depth thermal response have not been considered at this stage. An iso-thermal, non-catalytic, no-slip wall boundary condition is used for the steady flow calculation.

Table 1. Flow conditions used for computing mean-flow results.

$c_{N_2\infty} = 0.797$	$M_\infty = 15.3$
$c_{O_2\infty} = 0.200$	$p_\infty = 664\ Pa$
$c_{NO\infty} = 0.001$	$\rho_\infty = 7.83 \times 10^{-3}\ kg/m^3$
$c_{N\infty} = 0.001$	$Re_\infty = \rho_\infty U_\infty d/\mu_\infty = 26,480$
$c_{O\infty} = 0.001$	$r = 6.35 \times 10^{-3}\ m$

III. Flow Conditions

The conditions for this case are shown in Table 1. The blunt cone has a 7° half angle. During simulations, the body-surface is modeled as a no-slip wall with isothermal temperature $T_w = 1000\ K$. The axi-symmetric grid is $1106 \times 251 \times 2$, with exponential grid clustering near the wall in the wall-normal direction and algebraic clustering near the nose along the wall-tangential direction. This grid allows us to study the flow over the blunt cone from $0.0 < x/r < 63.3$, where $x/r = 0$ represents the stagnation point on the blunt cone, which corresponds to dimensional values $0.00\ m < x < 0.40\ m$.

IV. Mean Flow Results

Steady mean-flow results were computed using both the non-equilibrium and perfect gas models over the blunt cone. Figure 1 compares the shock shape for each gas model and corresponding experimental result[21] and computed perfect gas result from Candler[22]. Excellent agreement in both instances is displayed by our computed shock shapes. The scaled shock shape profile in the nose region is shown in Fig. 1(a), where it shows that the shock is pushed closer to the blunt cone surface in the non-equilibrium case due to its weaker shock. Figure 1(b) shows that the difference in shock stand-off distance extends downstream.

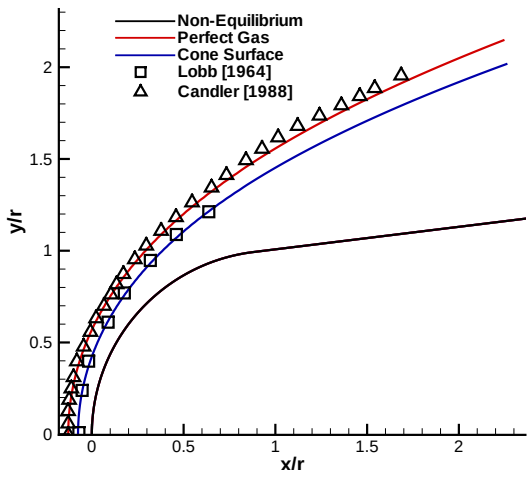

(a) Shock shape near nose of the cone.

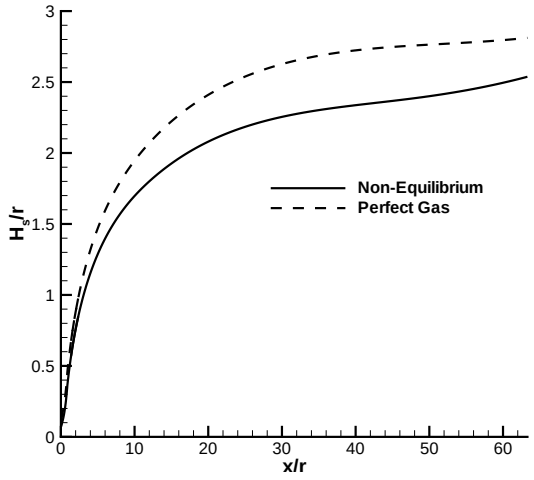

(b) Shock location. Note that the axes are not scaled and this is not a proper representation of the shock shape, but rather describes the coordinates of the shock location

Figure 1. Computed steady mean-flow shock shape and location.

Figure 2 compares the computed steady mean-flow temperature profiles along the stagnation line between the non-equilibrium and perfect gas models. The $x/r = 0$ value corresponds to the stagnation point on the blunt cone, and the left-most point for each curve represent values at the shock front. The translational temperature immediately across the shock is the same for both gas models due to the Rankine-Hugoniot relations. However, the translational temperature decreases sharply in the non-equilibrium case relative to the perfect gas case, as energy is lost in the vibrational energy relaxation and chemical reaction processes. The vibrational temperature is at its free-stream value immediately across

the shock but rises to over $7000\ K$ in overshooting the translational temperature. The iso-thermal wall condition sets each temperature value to $1000\ K$, but even near the wall, the vibrational temperature is in non-equilibrium with the translational temperature. The computed temperature contours near the nose for each case are shown in Fig. 3 and show that the non-equilibrium effects greatly affects the temperature throughout the flowfield.

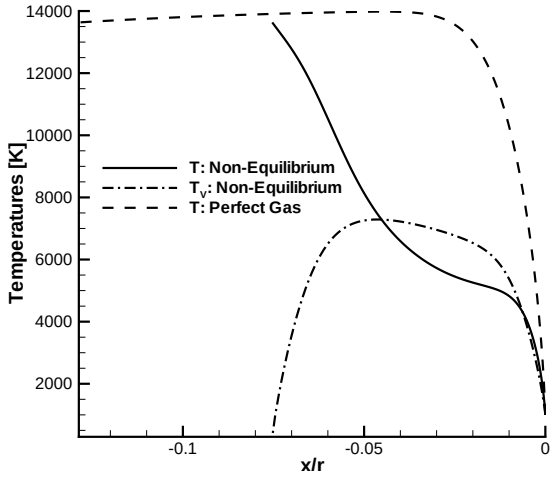

Figure 2. Computed steady mean-flow temperature profiles along stagnation line.

Figure 4 examines the chemical reaction processes in the non-equilibrium case. The species mass fractions along the stagnation line are shown in Fig. 4(a), where there is significant chemical activity associated with the high temperature gradients in the region. It is seen that as flow comes across the shock and encounters high temperatures, first, diatomic oxygen begins to dissociate, followed by dissociation of diatomic nitrogen, which leads to the production of monotonic oxygen, monotonic nitrogen, and nitric oxide. Near the wall, temperatures cool to the iso-thermal cold-wall value, which forces the recombination of some diatomic oxygen and nitrogen. The species mass fractions along the blunt cone surface are shown in Fig. 4(b). The most chemical activity occurs near the stagnation point at $x/r = 0$, which corresponds to the region with highest temperature gradients. However, the chemical composition is in non-equilibrium throughout the computational domain studied. As the flowfield temperature decreases downstream of the cone nose, there is recombination of diatomic oxygen and nitrogen.

The temperature profile of the two gas models at $x/r = 46.5$ is shown in Fig. 5(a). This again shows that the vibrational temperature is in non-equilibrium with the translational temperature inside the boundary layer. Figure 5(b) shows the velocity profile at $x/r = 46.5$. Figures 5(a)- 5(b) clearly show that the boundary layer thickness for the perfect gas model is greater than that of the non-equilibrium gas model. This difference in boundary layer thickness may be significant to the receptivity process, as the wavelength of the second mode disturbance is proportional to the boundary layer thickness[4]. Figure 6 displays the distribution of wall pressure along the surface of the blunt cone. Near the cone nose, the pressure in in the perfect gas case is higher than the non-equilibrium gas case due to the stronger shock, but the non-equilibrium effects on pressure are minimal.

V. Acoustic Disturbances

The receptivity of the hypersonic boundary layer to free-stream acoustic disturbance waves is studied. The disturbances are assumed to be weak planar fast acoustic waves in the free-stream before reaching the shock at zero incidence angle. The free-stream disturbances are superimposed on the steady mean-flow result to examine the receptivity process. The non-equilibrium real gas effects are studied by comparing the results from the perfect gas and non-equilibrium gas models. The perturbations of flow variables can be written as the summation of the mean-flow value and an oscillating component, Eq. 11.

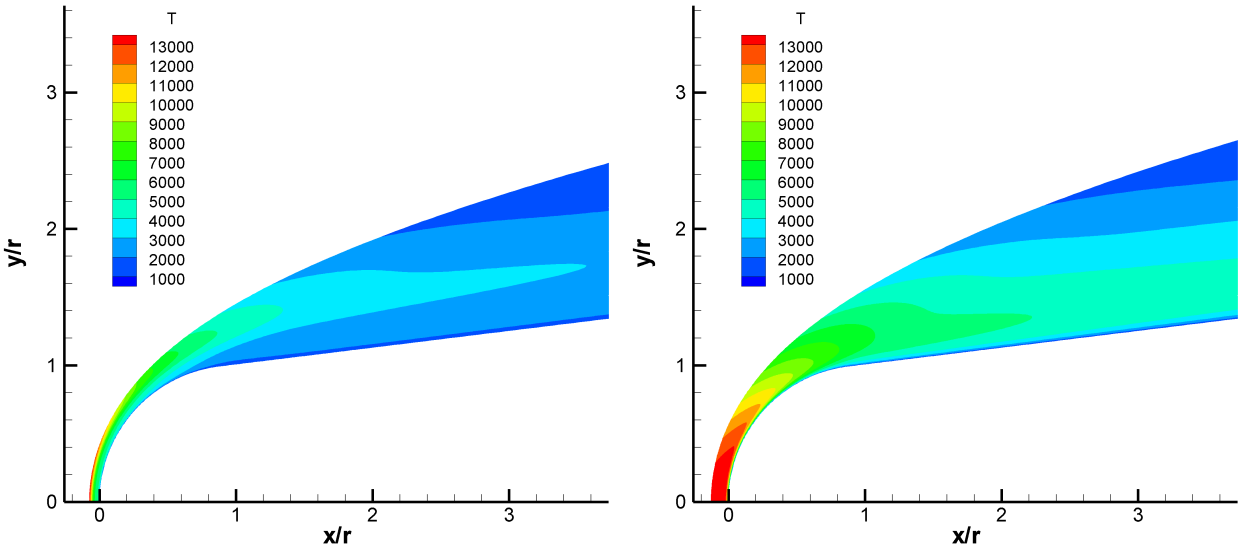

(a) Non-equilibrium gas.

(b) Perfect gas.

Figure 3. Computed steady mean-flow temperature contours.

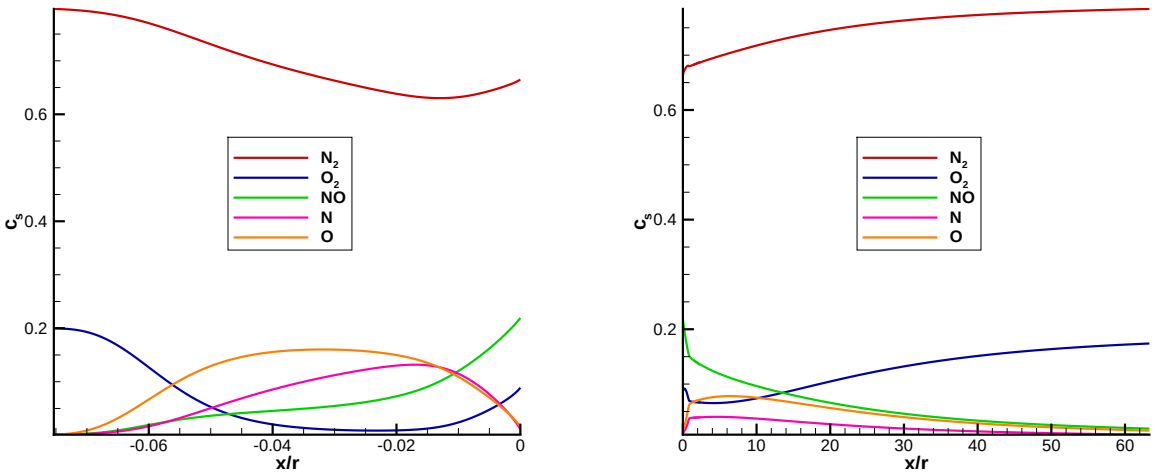

(a) Species mass fractions along stagnation line.

(b) Species mass fractions along blunt cone surface.

Figure 4. Computed steady mean-flow mass fractions.

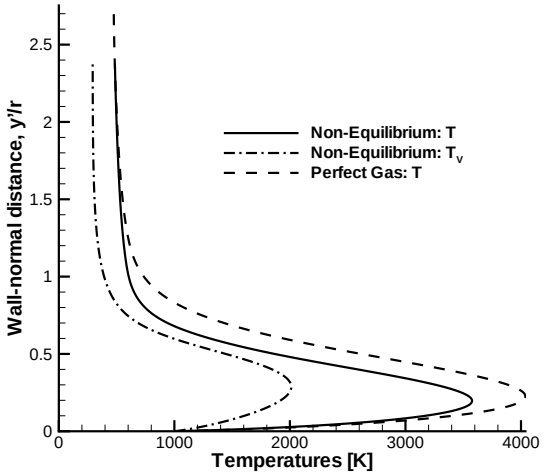

(a) Temperature profile.

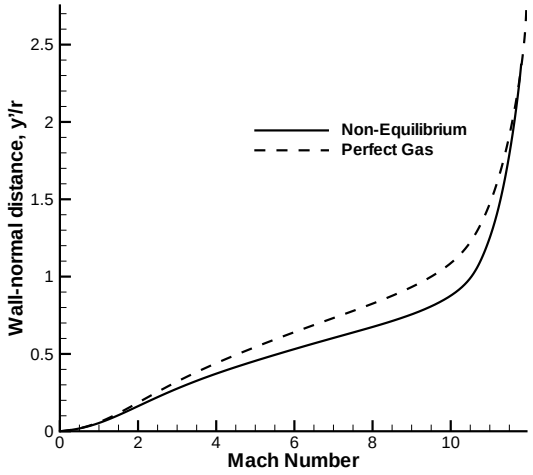

(b) Velocity profile.

Figure 5. Steady mean-flow profiles at $x/r = 46.5$.

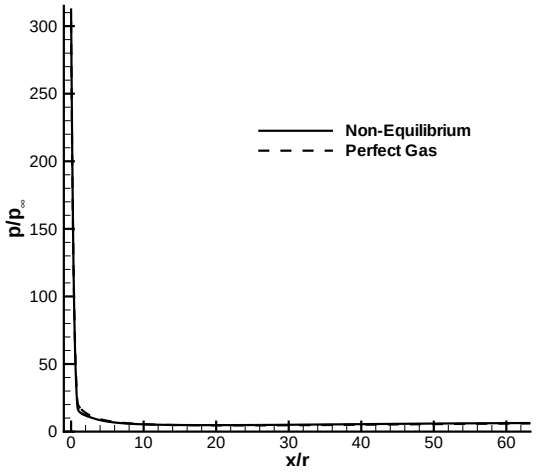

Figure 6. Steady mean-flow distribution of pressure along the wall surface.

$$V_\infty = \begin{bmatrix} \rho_{N_2,\infty} \\ \rho_{O_2,\infty} \\ \rho_{NO,\infty} \\ \rho_{N,\infty} \\ \rho_{O,\infty} \\ u_\infty \\ v_\infty \\ w_\infty \\ p_\infty \end{bmatrix} = \begin{bmatrix} \bar{\rho}_{N_2,\infty} \\ \bar{\rho}_{O_2,\infty} \\ \bar{\rho}_{NO,\infty} \\ \bar{\rho}_{N,\infty} \\ \rho_{O,\infty} \\ \bar{u}_\infty \\ \bar{v}_\infty \\ \bar{w}_\infty \\ \bar{p}_\infty \end{bmatrix} + \begin{bmatrix} \Delta\rho_{N_2} \\ \Delta\rho_{O_2} \\ \Delta\rho_{NO} \\ \Delta\rho_N \\ \Delta\rho_O \\ \Delta u \\ \Delta v \\ \Delta w \\ \Delta p \end{bmatrix} \cos\left(k_x x - \omega t\right). \tag{11}$$

The disturbance amplitudes for the imposed zero-incidence angle fast acoustic waves are defined by Eq. 12, where ϵ is a non-dimensional parameter representing the wave magnitude. For the zero-incidence angle case, the Δv and Δw amplitudes are each zero. The dimensionless frequency of the wave f^* is defined by Eq. 13.

$$\frac{\Delta p}{\gamma_\infty p_\infty} = \frac{\Delta\rho}{\rho_\infty} = \frac{\Delta u}{\gamma a_\infty} = \epsilon, \tag{12}$$

$$f^* = \frac{\omega\mu_\infty}{\rho_\infty u_\infty^2}, \tag{13}$$

$$\omega = k_x\left(u_\infty + a_\infty\right), \tag{14}$$

A. Shock-fitting procedure

Zhong's high-order finite-difference shock-fitting scheme[13] is the base solver used through this study. The details of this scheme are not presented in full here, but the inclusion of additional variables for the non-equilibrium gas case necessitates a re-derivation of components of the shock-fitting procedure, the details of which are presented here.

The flow variables immediately behind the shock are determined by the Rankine-Hugoniot relation,

$$F_s = F_\infty \tag{15}$$

where F is the flux in the computational space along the wall-normal grid line η, across the shock, and a characteristic compatibility equation from the flow field behind the shock. The subscript s denotes the values immediately behind the shock, and the subscript ∞ denotes the flux on the free-stream side of the shock surface. Their respective fluxes are found to be

$$F_s' = F_s \cdot \ell_s + V_s \ell_t, \tag{16}$$

$$F_\infty' = F_\infty \cdot \ell_\infty + V_\infty \ell_t, \tag{17}$$

where ℓ_s is the normal vector of the shock front and ℓ_t is the velocity of the shock front in the ℓ_s direction. With J as the Jacobian of the coordinate transform[13], these values are determined by

$$\ell_s = \left(\frac{\eta_x}{J}\right) i + \left(\frac{\eta_y}{J}\right) j + \left(\frac{\eta_z}{J}\right) k \tag{18}$$

$$\ell_t = \left(\frac{\eta_t}{J}\right). \tag{19}$$

Equations 15-17 combine to yield

$$\left(F_s - F_\infty\right) \cdot \ell_s + \left(V_s - V_\infty\right) \ell_t = 0. \tag{20}$$

Differentiating Eq. 20 with respect to time gives

$$\left(\frac{\partial F}{\partial \tau} - \frac{\partial F_\infty}{\partial \tau}\right) \cdot \ell_s + \left(\frac{\partial V_s}{\partial \tau} - \frac{\partial V_\infty}{\partial \tau}\right) \ell_t + \left(F_s - F_\infty\right) \cdot \frac{\partial \ell_s}{\partial \tau} + \left(V_s - V_\infty\right) \frac{\partial \ell_t}{\partial \tau} = 0 \tag{21}$$

In the steady case in which no disturbances are introduced in the free-stream, the derivatives of the free-stream values with respect to time are inherently zero. In an unsteady free-stream, however, the derivative of the disturbance with respect to time is therefore

$$\frac{\partial V_\infty}{\partial \tau} = \left[\omega \cdot \Delta V - \Delta V \left(k_x x_\tau\right)\right] \sin\left(k_x x - \omega t\right). \tag{22}$$

Equation 21 is rewritten as

$$B'_s \frac{\partial V_s}{\partial \tau} - B'_\infty \frac{\partial V_\infty}{\partial \tau} + \left(F_s - F_\infty\right) \cdot \frac{\partial \ell_s}{\partial \tau} + \left(V_s - V_\infty\right) \frac{\partial \ell_t}{\partial \tau} = 0, \tag{23}$$

where B'_∞ is the flux Jacobian,

$$B' = \frac{\partial F'}{\partial V}. \tag{24}$$

The flux Jacobian for the freestream values is given in Eq. 26, with Eqs. 26- 31 defining the parameters within the flux Jacobian.

$$B'_\infty = \begin{bmatrix} u'_n & 0 & 0 & \cdots \\ 0 & u'_n & 0 & \\ 0 & 0 & u'_n & \\ 0 & 0 & 0 & \\ 0 & 0 & 0 & \\ uu'_n & uu'_n & uu'_n & \\ vu'_n & vu'_n & vu'_n & \\ wu'_n & wu'_n & wu'_n & \\ \left(\alpha + h_{N_2} + e_{V,N_2} + \beta\right) u'_n & \left(\alpha + h_{O_2} + e_{V,O_2} + \beta\right) u'_n & \left(\alpha + h_{NO} + e_{V,NO} + \beta\right) u'_n & \\ \left(e_{V,N_2} + \beta\right) u'_n & \left(e_{V,O_2} + \beta\right) u'_n & \left(e_{V,NO} + \beta\right) u'_n & \end{bmatrix}$$

$$\begin{bmatrix} 0 & 0 \\ 0 & 0 \\ 0 & 0 \\ u'_n & 0 \\ 0 & u'_n \\ uu'_n & uu'_n \\ vu'_n & vu'_n \\ wu'_n & wu'_n \\ \left(\alpha + h_N + \beta\right) u'_n & \left(\alpha + h_O + \beta\right) u'_n \\ \beta u'_n & \beta u'_n \end{bmatrix} \quad \cdots \quad \begin{bmatrix} \rho_{N_2} n_x & \rho_{N_2} n_y & \rho_{N_2} n_z & 0 \\ \rho_{O_2} n_x & \rho_{O_2} n_y & \rho_{O_2} n_z & 0 \\ \rho_{NO} n_x & \rho_{NO} n_y & \rho_{NO} n_z & 0 \\ \rho_N n_x & \rho_N n_y & \rho_N n_z & 0 \\ \rho_O n_x & \rho_O n_y & \rho_O n_z & 0 \\ \rho u n_x + \rho u'_n & \rho u n_y & \rho u n_z & n_x \\ \rho v n_x & \rho v n_y + \rho u'_n & \rho v n_z & n_y \\ \rho w n_x & \rho w n_y & \rho w n_z + \rho u'_n & n_z \\ \left(E + p\right) n_x + \rho u'_n u & \left(E + p\right) n_y + \rho u'_n v & \left(E + p\right) n_z + \rho u'_n w & \left(\frac{1}{\gamma - 1} + \psi\right) u'_n + u_n \\ E_V n_x & E_V n_y & E_V n_z & \psi u'_n \end{bmatrix} \tag{25}$$

$$\alpha = \frac{1}{2}\left(u^2 + v^2 + w^2\right) \tag{26}$$

$$\beta = \sum_s \left(\rho_s \frac{\partial e_{V,s}}{\partial \rho}\right) = \sum_s \left(\rho_s \frac{\partial e_{V,s}}{\partial T} \frac{\partial T}{\partial \rho}\right) \tag{27}$$

$$\psi = \frac{\partial E_V}{\partial p} = \sum_s \left(\rho_s \frac{\partial e_{V,s}}{\partial p}\right) = \sum_s \left(\rho_s \frac{\partial e_{V,s}}{\partial T} \frac{\partial T}{\partial p}\right) \tag{28}$$

$$\frac{\partial e_{V,s}}{\partial T} = \frac{\partial}{\partial T}\left\{\frac{R_{univ}}{M_s}\frac{\theta_{V,s}}{e^{\theta_{V,s}/T}-1}\right\} = e_{V,s}\frac{M_s e^{\theta_{V,s}/T}}{R_{univ}T^2} \tag{29}$$

$$\frac{\partial T}{\partial \rho} = \frac{-p}{\rho^2 R} \tag{30}$$

$$\frac{\partial T}{\partial p} = \frac{1}{\rho R} \tag{31}$$

The corresponding left eigenvector of the flux Jacobian matrix is found in Eq. 32. With Eqs. 26 and 32, the Zhong shock-fitting scheme can be solved for the non-equilibrium gas model.

$$l_N = \begin{bmatrix} \frac{\gamma-1}{2}\left(\alpha - h^0_{N_2}\right) - au_n + \left(R_{N_2} - \frac{\gamma-1}{2}c_{v,N_2}\right)T \\ \frac{\gamma-1}{2}\left(\alpha - h^0_{O_2}\right) - au_n + \left(R_{O_2} - \frac{\gamma-1}{2}c_{v,O_2}\right)T \\ \frac{\gamma-1}{2}\left(\alpha - h^0_{NO}\right) - au_n + \left(R_{NO} - \frac{\gamma-1}{2}c_{v,NO}\right)T \\ \frac{\gamma-1}{2}\left(\alpha - h^0_{N}\right) - au_n + \left(R_{N} - \frac{\gamma-1}{2}c_{v,N}\right)T \\ \frac{\gamma-1}{2}\left(\alpha - h^0_{O}\right) - au_n + \left(R_{O} - \frac{\gamma-1}{2}c_{v,O}\right)T \\ -\frac{\gamma-1}{2}u + an_x \\ -\frac{\gamma-1}{2}v + an_y \\ -\frac{\gamma-1}{2}w + an_z \\ \frac{\gamma-1}{2} \\ -\frac{\gamma-1}{2} \end{bmatrix} \tag{32}$$

VI. Receptivity to Planar Fast Acoustic Waves

Free-stream fast acoustic waves expected to excite the unstable second Mack mode are studied. The non-dimensional free-stream disturbance amplitude is chosen to be $\epsilon = 5.0 \times 10^{-4}$, which is small enough such that the forcing waves are considered linear. A non-dimensional frequency of $f^* = 2.2 \times 10^{-4}$ is used. Given the free-stream conditions, this non-dimensional frequency gives an acoustic wavelength of approximately two boundary layer thicknesses, which is a good first guess in the absence of a corresponding LST analysis at the prediction of a second-mode instability inducing frequency.

Figure 7 shows instantaneous pressure perturbations for both the non-equilibrium and perfect gas cases. It is clear that the free-stream disturbances pass through the shock and are seen by the entire flowfield. Additionally, the acoustic waves run nearly parallel to the surface of the cone. However, the wave structure of the perturbations in the boundary layer differ from the structure seen in the inviscid region. Near the nose, perturbations along the wall are the most significant, as shown in Fig. 8. The wave structures are generally similar for both gas models. However, in the up-stream region, the pressure perturbation amplitudes are greater for the non-equilibrium gas case and confined to a region closer to the wall, due to the smaller boundary layer in the non-equilibrium case. These wall perturbations decay significantly towards the computational exit boundary, as shown in Fig. 9.

The instantaneous temperature perturbations for each case are shown in Fig. 10. The contours show a so-called "rope" like wave structure that resides on the edge of the boundary layer in the downstream region. In the upstream region, as shown in Fig. 11, it is seen that the forcing waves from the freestream pass through the shock and enter the boundary layer to generate mode I waves in the boundary layer. These waves decay as flow moves downstream. Figure 12 shows that, near the computational domain exit, the "rope" like wave structure at the edge of the boundary layer is the dominant perturbation.

Figure 13 shows instantaneous pressure perturbation along the blunt cone wall surface. The perturbation is non-dimensionalized by the local steady mean-flow pressure value. Pressure perturbations display complex wave patterns, indicating the presence of several wave modes generated in the boundary layer. It is noted that the maximum amplitude for the non-equilibrium perturbation is higher than that of the perfect gas case, and the stable downstream perturbation amplitude is higher for the non-equilibrium case as well.

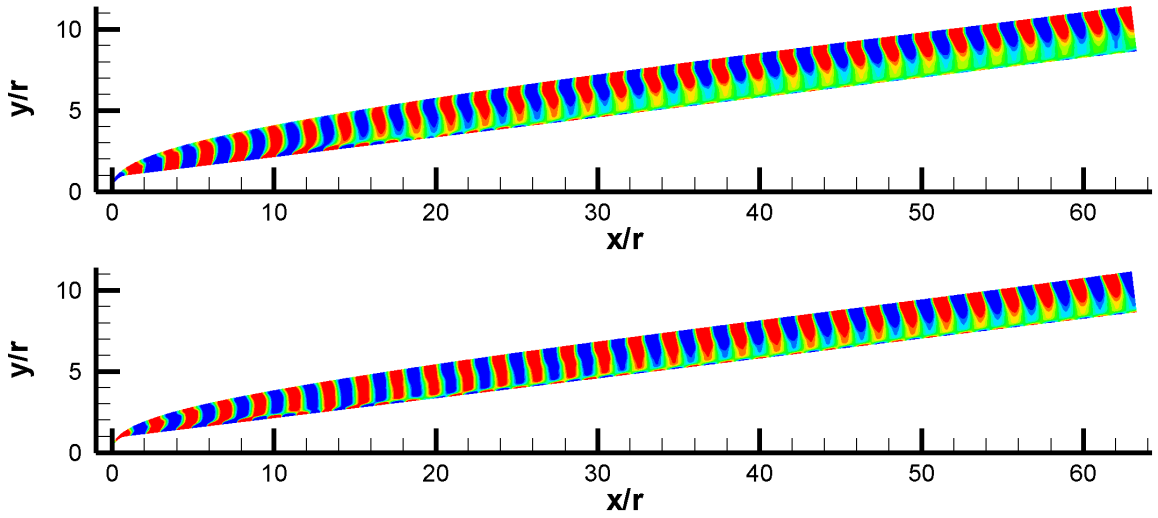

Figure 7. Instantaneous pressure perturbation contours induced by planar fast acoustic wave for the perfect gas case [TOP] and non-equilibrium gas case [BOTTOM]. Refer to Figs. 8- 9 for contour levels.

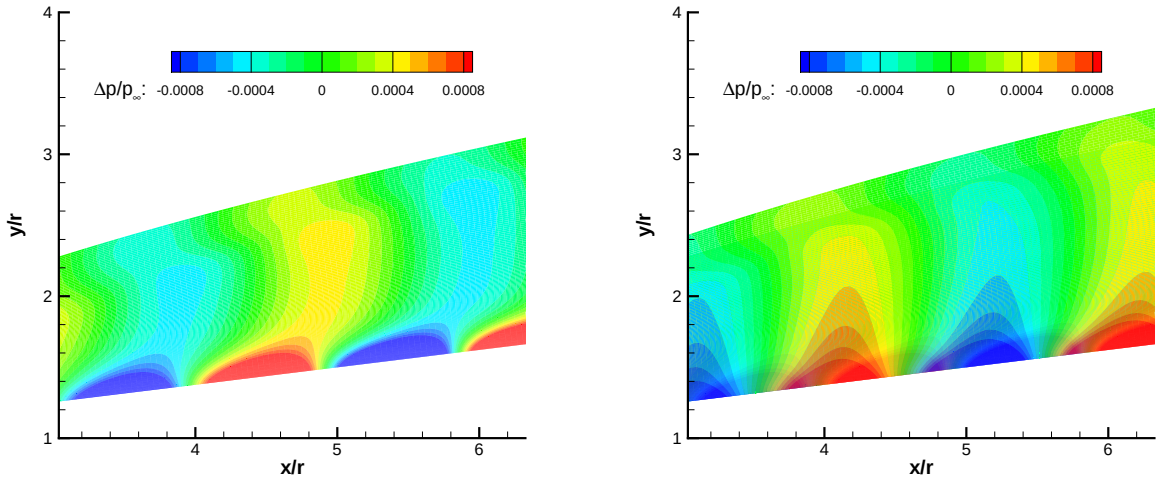

(a) Non-equilibrium gas.

(b) Perfect gas.

Figure 8. Instantaneous pressure perturbation contours induced by planar fast acoustic wave in a localized upstream region.

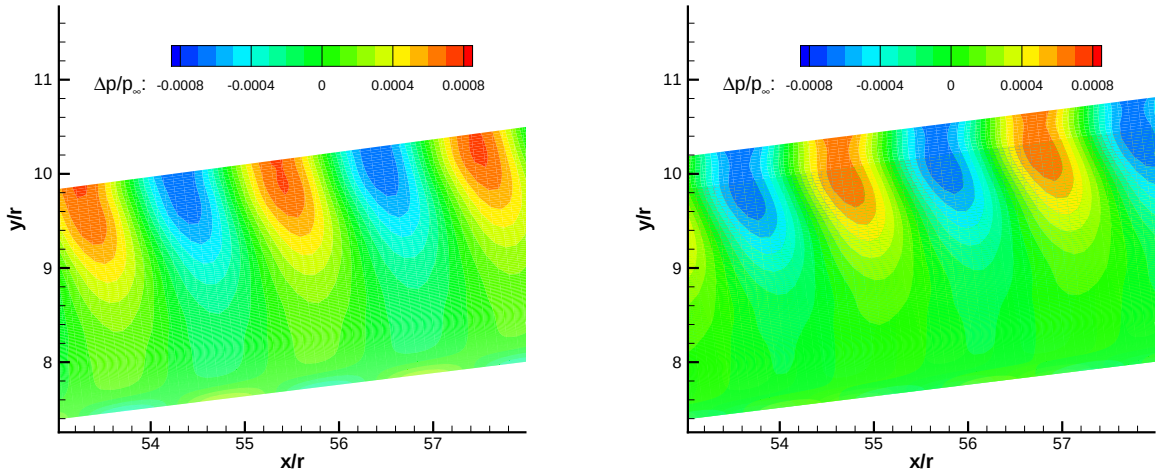

(a) Non-equilibrium gas.

(b) Perfect gas.

Figure 9. Instantaneous pressure perturbation contours induced by planar fast acoustic wave in a localized downstream region.

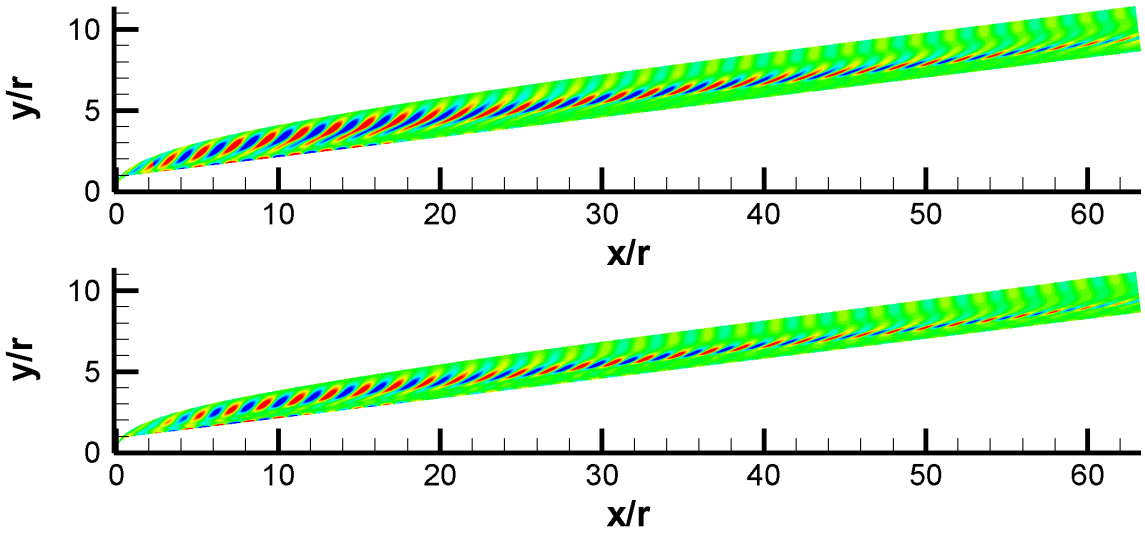

Figure 10. Instantaneous temperature perturbation contours induced by planar fast acoustic wave for the perfect gas case [TOP] and non-equilibrium gas case [BOTTOM]. Refer to Figs. 11- 12 for contour levels.

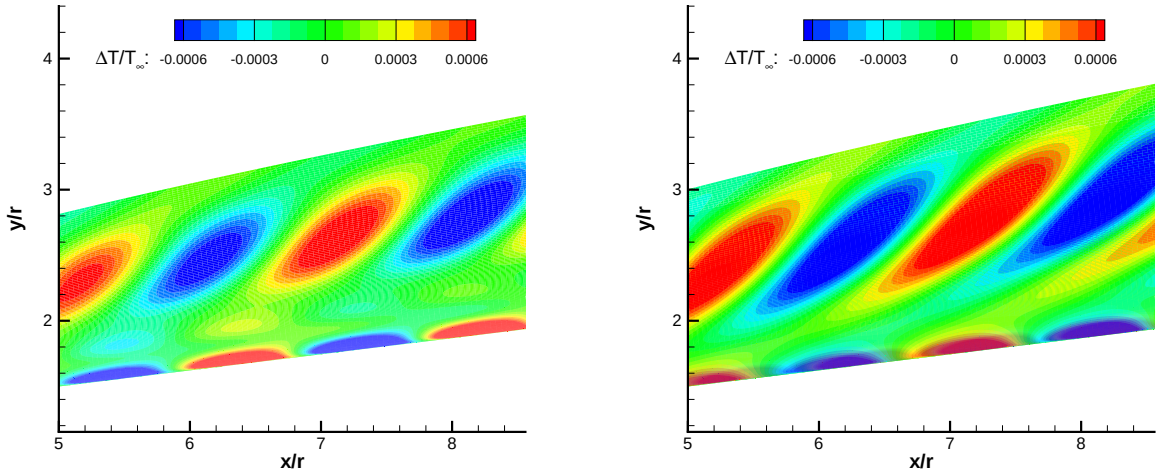

(a) Non-equilibrium gas. (b) Perfect gas.

Figure 11. Instantaneous temperature perturbation contours induced by planar fast acoustic wave in a localized upstream region.

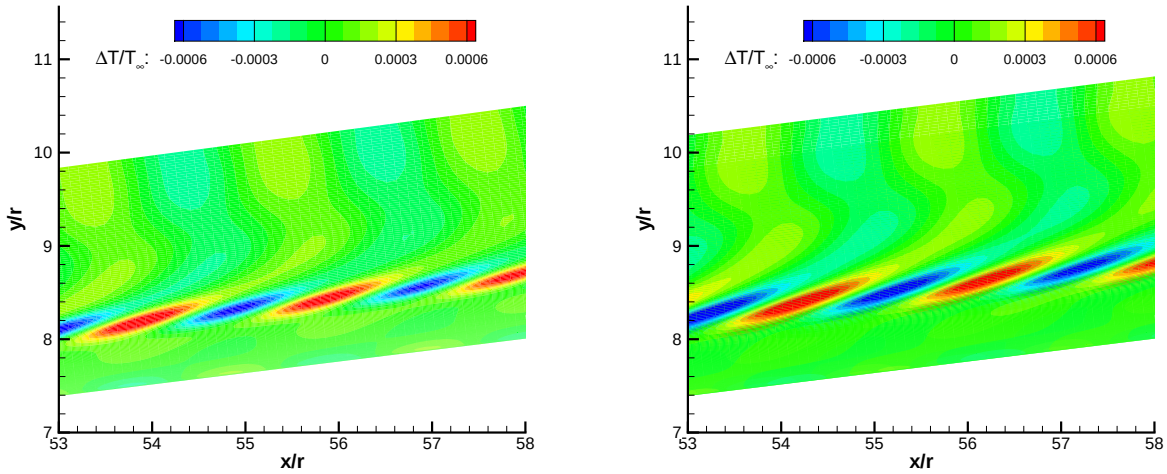

(a) Non-equilibrium gas. (b) Perfect gas.

Figure 12. Instantaneous temperature perturbation contours induced by planar fast acoustic wave in a localized downstream region.

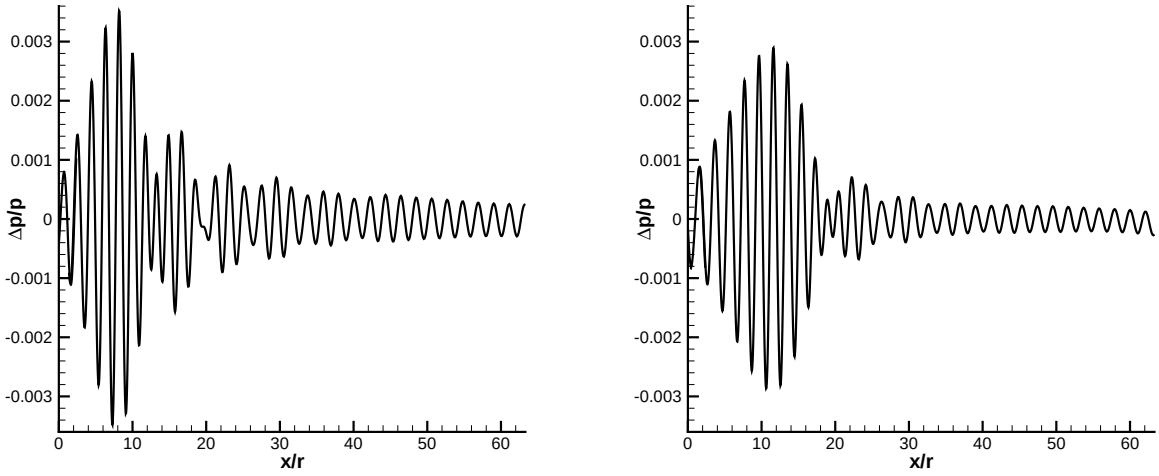

(a) Non-equilibrium gas.

(b) Perfect gas.

Figure 13. Instantaneous pressure perturbation along the cone surface.

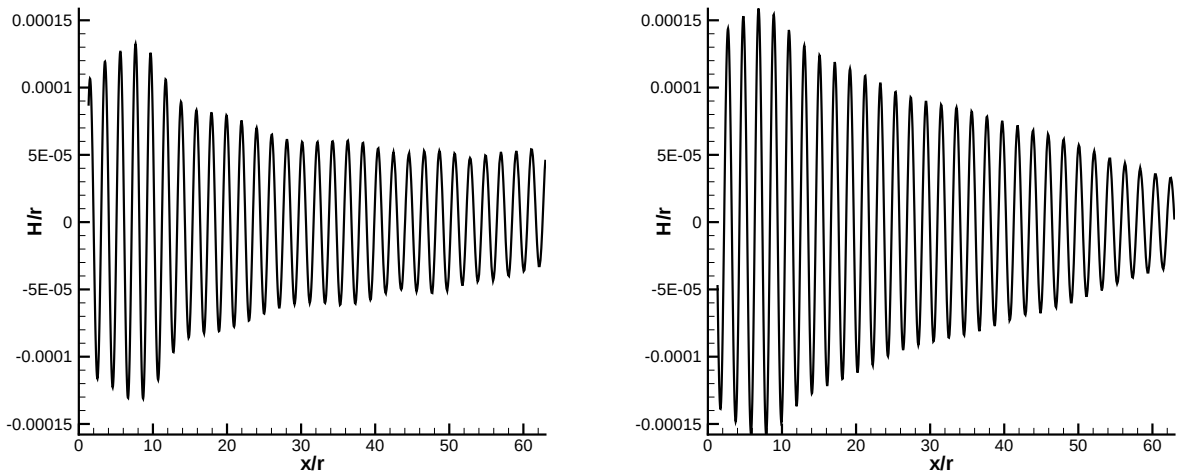

(a) Non-equilibrium gas.

(b) Perfect gas.

Figure 14. Instantaneous shock perturbations induced by planar fast acoustic wave.

Figure 14 shows instantaneous shock height perturbation for each gas model. It is found that the shock oscillations are, in general, not significant and relatively small in magnitude. However, for both gas models, the shock height oscillates much more in the region near the blunt nose and perturbations decay moving downstream.

By taking the Fourier transform of the data, the amplitude of the perturbations throughout the flowfield can be constructed. Figure 15 shows the distribution of pressure disturbance amplitudes along different streamwise grid lines, where $j = 1$ corresponds to the cone wall, $j = 51$ is within the boundary layer, $j = 101$ is near the edge of the boundary layer, and $j = 201$ is near the shock front. It can be seen that the perturbation amplitudes can vary greatly across different grid lines. Within the boundary layer, the complex wave structures are apparent and similar in shape. The maximum amplitude for each gas case occurs within the boundary layer at the stagnation point, as shown in Fig. 15(a). The maximum amplitude past the blunt nose occurs along the wall at approximately $x/r = 7$ for the non-equilibrium case and $x/r = 11$ for the perfect gas case. Just outside the boundary layer along the $j = 101$ grid line, the amplitudes are significantly lower than those within the boundary layer. However, the forcing amplitudes are apparent and relatively steady near the shock throughout the flowfield, as seen along the $j = 201$ grid line. The amplitude along each grid line for each case decays going downstream and shows no signs of growth at the computational exit boundary. It is noted that throughout the flowfield, with the exception of the stagnation point, the amplitudes for the non-equilibrium case are greater than those for the perfect gas case.

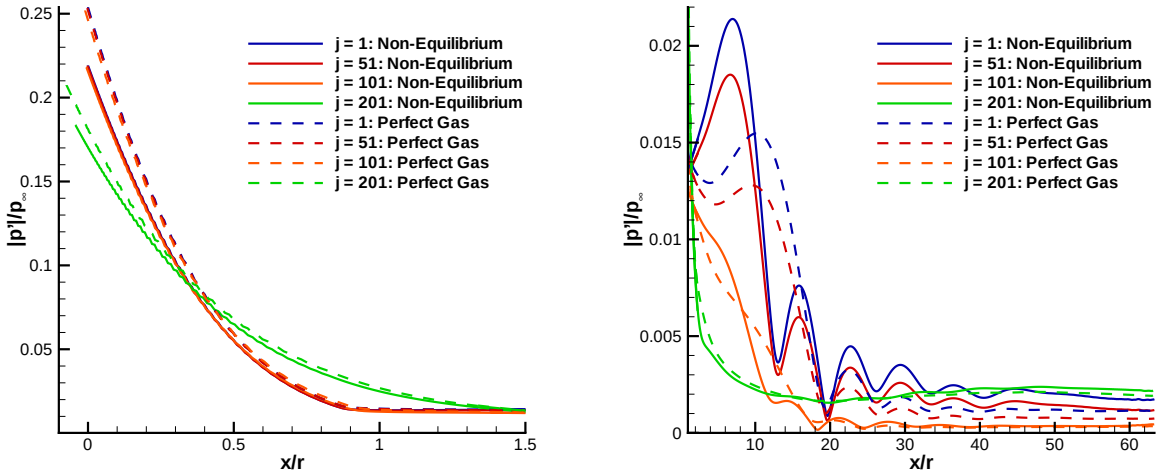

(a) Region near cone nose.

(b) Downstream the nose.

Figure 15. Distribution of pressure perturbation along different grid lines induced by planar fast acoustic wave.

The distribution of the Fourier amplitudes of temperature perturbations along different grid lines are shown in Fig. 16. Similar behavior to the pressure perturbation amplitudes is observed. Within the boundary layer, complex wave structures are observed, with the maximum amplitudes occurring along the wall and amplitudes decaying downstream. There are no signs of unstable growth at the computational boundary exit. Again, the non-equilibrium gas case shows higher perturbation amplitudes than the perfect gas case.

VII. Conclusions

Hypersonic receptivity was examined for Mach 15.3 flow over a blunt cone with nose radius 6.35×10^{-3} m and half angle 7° and imposed free-stream fast acoustic wave disturbances using a high-order shock-fitting finite-difference solver. This was studied by first computing a steady mean-flow result, then super-imposing a free-stream fast acoustic wave. Results were computed for flows using both thermochemical non-equilibrium and perfect gas models and were then compared to determine the non-equilibrium effect. Complex wave structures were found in the boundary layer for each gas model when a free-stream acoustic disturbance wave was introduced. The non-equilibrium gas case has higher perturbation amplitudes within the boundary layer and has its maximum perturbation amplitude nearer the

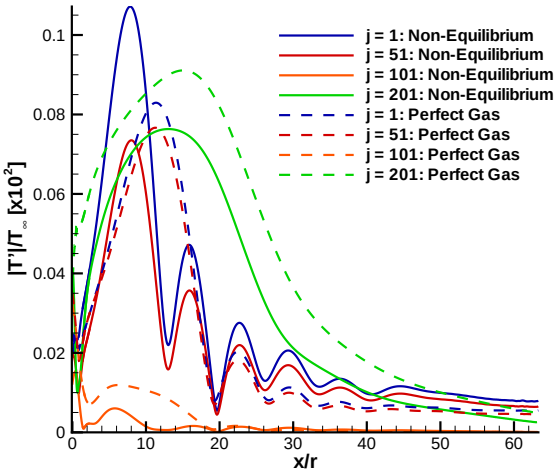

Figure 16. Distribution of temperature perturbation along different grid lines induced by planar fast acoustic wave.

blunt nose than the perfect gas case. These findings indicate that non-equilibrium effects destabilize the boundary layer. However, downstream unstable growth modes were not observed in our study. Future work will incorporate a more thorough receptivity study. This will include a linear stability analysis to predict the unstable free-stream frequency range and accompanying unstable growth region. Then, further DNS studies of the receptivity process will be investigated to capture and identify the various wave modes within the boundary layer.

Acknowledgments

N. Parsons would like to thank his colleagues Xiaowen Wang and Akshay Prakash for their collaboration in the development of the code used in this study. This research is funded by NASA award NNX08AB39A and by the AFOSR/NASA National Center for Hypersonic Research in Laminar-Turbulent Transition.

References

[1]Mack, L., "Boundary Layer Linear Stability Theory," *AGARD report No. 709*, 1984, pp. 1–81.

[2]Malik, M. R., "Numerical Methods for Hypersonic Boundary Layer Stability," *Journal of Computational Physics*, Vol. 86, 1990, pp. 376–413.

[3]Stuckert, G. and Reed, H. L., "Linear Disturbances in Hypersonic, Chemically Reacting Shock Layers," *AIAA Journal*, Vol. 32, No. 7, 1994.

[4]Hudson, M. L., Chokanid, N., and Candler, G., "Linear Stability of Hypersonic Flow in Thermochemical Nonequilibrium," *AIAA Journal*, Vol. 35, No. 6, 1997.

[5]Johnson, H. G., Seipp, T. G., and Candler, G. V., "Numerical study of hypersonic reacting boundary layer transition on cones," *Physics of Fluids*, Vol. 10, No. 10, Oct. 1998.

[6]Germain, P. and Hornung, H. G., "Transition on a Slender Cone in Hypervelocity Flow," *Experiments in Fluids*, Vol. 22, Oct. 1997, pp. 183–190.

[7]Martin, M. P. and Candler, G. V., "Effect of chemical reactions on decaying isotropic turbulence," *Physics of Fluids*, 1998.

[8]Ma, Y. and Zhong, X., "Receptivity to Freestream Disturbances of a Mach 10 Nonequilibrium Reacting Oxygen Flow over a Flat Plate," *AIAA 2004-0256*.

[9]Stemmer, C., "Hypersonic Transition Investigations In A Flat-Plate Boundary-Layer Flow at M=20," *AIAA 2005-5136*.

[10]Zhong, X., "Receptivity of Mach 6 Flow Over a Flared Cone to Freestream Disturbance," *42nd AIAA Aerospace Sciences Meeting and Exhibit*, Jan. 2004.

[11]Zhong, X. and Ma, Y., "Receptivity and Linear Stability of Stetson's Mach 8 Blunt Cone Stability Experiments," *32nd AIAA Fluid Dynamics Conference and Exhibit*, June 2002.

[12]Zhong, X., "Leading-edge receptivity to free-stream disturbance waves for hypersonic flow over a parabola," *Journal of Fluid Mechanics*, Vol. 441, 2001, pp. 315–367.

[13]Zhong, X., "High-order finite-difference schemes for numerical simulation of hypersonic boundary-layer transition," *Journal of Computational Physics*, Vol. 144, No. 2, Aug. 1998, pp. 662–709.

[14]Prakash, A., Parsons, N., Wang, X., and Zhong, X., "High Order Numerical Simulation of Hypersonic Flow over Blunt Bodies with Chemical and Thermal Non-equilibrium," *AIAA 40th Fluid Dynamics Conference and Exhibit*, June 2010.

[15]Millikan, R. C. and White, D. R., "Systematics of Vibrational Relaxation," *Journal of Chemical Physics*, Vol. 39, No. 12, Dec. 1963.

[16]Park, C., "On Convergence of Computation of Chemically Reacting Flows," *AIAA 1985-0247*.

[17]Park, C., "Review of Chemical-Kinetic Problems of Future NASA Missions, I: Earth Entries," *Journal of Thermophysics and Heat Transfer*, Vol. 3, pp. 385–398.

[18]McBride, B., Zehe, M., and Gordon, S., "NASA Glenn Coefficients for Calculating Thermodynamic Properties of Individual Species," Nasa tp 2002-211556, Cleveland, Ohio.

[19]Gupta, R. N., Yos, J. M., Thompson, R. A., and Lee, K., "A Review of Reaction Rates and Thermodynamic Transport Properties for an 11-species Air Model for Chemical and Thermal Nonequilibrium Calculations to 30000 K," Nasa reference publication 1232.

[20]Ramshaw, J. D., "Self-Consistent Effective Binary Diffusion in Multicomponent Gas Mixtures," *Journal of Non-Equilibrium Thermodynamics*, Vol. 15, No. 3, 1990, pp. 295–300.

[21]Lobb, R. K., "Experimental Measurement of Shock Detachment Distance on Spheres Fire in Air at Hypervelocities," Tech. rep., ed. W.C. Nelson, Pergammon Press, MacMillan Co, New York.

[22]Candler, G., "The computation of weakly ionized hypersonic flows in thermo-chemical nonequilibrium," June, 1988, PhD thesis.